International Symposium
On Turbulence and Shear Flow
Phenomena (TSFP-9)
June 30 - July 3, 2015 *Melbourne, Australia*

GEOMETRY EFFECT OF ISOLATED ROUGHNESS ON BOUNDARY LAYER TRANSITION INVESTIGATED BY TOMOGRAPHIC PIV

Qingqing Ye
Department of Aerodynamics
Delft University of Technology
Kluyverweg 2, 2629HT Delft, the Netherlands
q.ye-1@tudelft.nl

Ferry F.J Schrijer
Department of Aerodynamics
Delft University of Technology
Kluyverweg 2, 2629HT Delft, the Netherlands
f.f.j.schrijer@tudelft.nl

Fulvio Scarano
Department of Aerodynamics
Delft University of Technology
Kluyverweg 2, 2629HT Delft, the Netherlands
f.scarano@tudelft.nl

ABSTRACT

Transitional flow over isolated roughness elements is investigated in the incompressible flow regime using Tomographic PIV. Three different geometries are considered (micro-ramp, cylinder and square) with same height and span. Their effect on accelerating boundary layer transition is compared and discussed. The measurement domain encompasses the full transition process and the flow development until the turbulent regime is established. The mean flow topology reveals a single pair of streamwise vortices for the micro-ramp as opposed to the additional pair associated to the horseshoe vortex around cylindrical and square elements. The statistical analysis of velocity fluctuations indicates a transition process induced from the point where the streamwise vortices induce an inflexional velocity profile. The cascade progresses downstream with a localized fluctuations increase at the turbulent-non-turbulent interface. The instantaneous flow topology contributes in explaining the transition mechanism, which appears to be dominated by hairpin-like vortices concentrating at the laminar-turbulent interface.

INTRODUCTION

Roughness induced boundary layer transition is an active research topic due to its significance for aerodynamic and aero-thermodynamic performance. A roughness element present in a laminar boundary layer may act as source of disturbance potentially accelerating the transition process. The element induces both streamwise and spanwise vortices in the wake region, resulting in inflection points in the velocity profile in spanwise and wall-normal directions (Rizzetta and Visbal. 2007). The effectiveness of a roughness element in promoting transition strongly depends not only on Reynolds number, roughness size, but also on its shape (Klenbanoff et al. 1992). The flow pattern around different types of isolated roughness elements has been investigated in both subsonic and supersonic flows. Acarlar and Smith (1987) observed hairpin vortices formed in the separated shear layer behind a hemispherical element. Such vortices plays a significant role on the progress of transition. Ergin and White (2006) performed measurements in the wake of an array of cylinders by means of hot-wire anemometry in subsonic flow and found the growth of streamwise velocity fluctuations which leads to transition is ascribed to the presence of Kelvin-Helmholz (K-H) instability. The onset of K-H instability in the wake of a micro-ramp was also observed in experimental (Sun et al, 2012) and numerical (Li and Liu. 2010) investigations in supersonic turbulent boundary layer. In a supersonic laminar boundary layer, Iyer et al (2013) used DNS to study the wake of cylinder and found that the source of unsteadiness depends on the flow condition (Mach and Reynolds number). By performing a stability analysis, Choudhari et al (2010) clarified that streak instabilities dominate the flow downstream of the cylinder, square and hemisphere, while shear layer instability is not as important.

The discussion remains open on which factor of the roughness geometry is more directly determining its effectiveness in promoting transition. Most studies deal directly with the most relevant high-speed regime (Danehy et al. 2010, Tirtey et al. 2011). The present study puts the attention to the transition process in the low-speed regime, where compressibility effects do not play a role and the topology of the flow can be studied in its details to determine the flow pattern of transition.

Three different geometries for isolated roughness are considered with the main objective of comparing the early stages of transition. The investigation makes use of Tomographic particle image velocimetry (PIV) to depict the velocity field in a three-dimensional domain. The measurement domain covers a large spanwise and streamwise range in order to follow the evolution of vortical structures and transition process. The experiments conducted at a supercritical roughness height based Reynolds number (Re_h=1140). The results show different transitional flow patterns emanating from the roughness

elements. The cross-flow topology identifies the mean structure of streamwise vortices embedded in the wake. The statistical evaluation of the velocity fluctuations yields the distinction between the turbulent and laminar flow regions. The details of unsteady flow activity at the boundaries are inspected by instantaneous visualization with the aid of the vortex detection λ_2 criterion.

EXPERIMENTAL CONFIGURATION

The experiments were carried out in the low speed wind tunnel (W-tunnel, 0.4×0.4m^2 test section) of the Aerodynamics Laboratories of the Aerospace Engineering Department at TU Delft. An aluminum flat plate with a length of 700mm, span of 400mm and a thickness of 10mm is installed in the mid-plane of the test section. The plate leading edge has super elliptic profile, preventing flow separation and curvature discontinuity. The plate surface was covered by black-matt adhesive foil to reduce the laser reflections during the PIV measurements. The roughness elements (micro-ramp, cylinder and square) with a height (h) of 2mm and span width (c) of 4mm were installed on the centerline and 290mm downstream of the leading edge. The length (l) of micro-ramp is 4.5mm. A schematic layout of the elements is shown in Figure 1.

The experiments were conducted at a free stream velocity of 10m/s. The corresponding Reynolds number based on ramp-height (Re_h=u_h×h/υ) is 1140. At the ramp position, the undisturbed laminar boundary layer thickness (δ_{99}) is 3.1mm. The resulting ratio between roughness height and boundary layer thickness is h/δ=0.65. The shape factor of the undisturbed boundary layer is 2.6, indicating the laminar regime.

In the present Tomographic PIV measurement, the flow was seeded with a SAFEX fog machine that generates water-glycol droplets of approximately 1µm diameter. The seeding concentration is carefully adjusted at approximately 4 particles/mm^3. Pulsed illumination is obtained with a Quantel *CFR PIV-200* Nd: YAG laser (200mJ/pulse, 532nm wavelength, 9ns pulse duration) with pulse separation time setting to 30µs. The free stream particle displacement is 10 pixels. An array of four LaVision Imager Pro LX interline CCD cameras (4872×3248pixels, 7.4µm/pixel) was arranged subtending an arc to simultaneously record the images of the light scattered by the tracers in the illuminated region, as shown in Figure 2. Objectives of 105mm focal length are mounted at an angle to comply with the Scheimpflug conditions. The numerical aperture was set at $f_\#$=11, resulting in a focal depth of 8.4mm. The sensor was cropped in the vertical direction resulting in an active sensor region of 4872×1500 pixels. The corresponding measurement volume size is 150(x)×6(y)×46(z)mm^3 (75h×3h×23h). Each dataset consists of 200 snapshots acquired at 1.5Hz rate.

System synchronization, data acquisition and processing is obtained with LaVision Davis 8 software. The 3D calibration of the tomographic system establishing the relation between the three-dimensional domain (object space) and its projection onto the camera sensor (image space) is obtained with a self-made target and refined with the 3D self-calibration technique. The raw images were pre-processed by the subtraction of pixel time-minimum and of the spatial minimum from a kernel of 31×31 pixels. Image intensity was homogenized by normalization against the local average (kernel of 51×51 pixels). The measurement volume was reconstructed by using the CSMART. Volume correlation was based on 3D spatial cross-correlation with multi-grid and volume deformation analysis until a final interrogation volume of 48×20×48 voxels (1.4×0.6×1.4 mm^3), with an overlap of 75% between neighboring interrogation windows. Outliers were removed by using the normalized median filter and replaced by linear interpolation of the surrounding vectors.

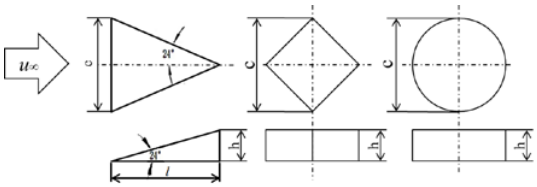

Figure 1. Geometry of the roughness elements, left: micro-ramp, middle: square, right: cylinder.

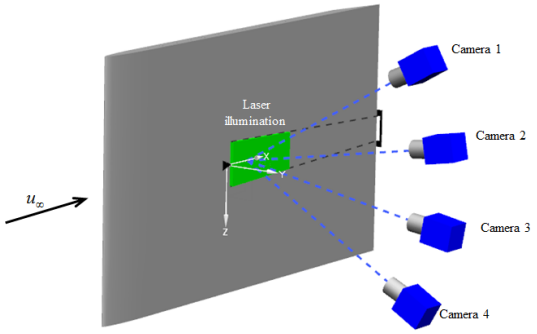

Figure 2. Schematic representation of measurement setup.

MEAN FLOW TOPOLOGY

The mean flow organisation for different roughness elements is obtained by averaging the 200 uncorrelated instantaneous snapshots. The cross-flow field is inspected at two y-z planes positioned downstream of the roughness (x/h=5, 15). Results are illustrated in Figure 3, where the projection of the streamlines on the y-z plane is visualized with the color contours of streamwise velocity (u/u_∞).

In the near wake region (x/h=5), micro-ramp induces a lateral downwash and a pair of counter rotating vortices which produce a central upwash motion shown with the projected streamlines in Figure 3(a). This pattern has been reported in studies conducted in supersonic turbulent boundary layers (Sun et al. 2012). The pronounced upwash motion induced by this primary vortex pair is associated to a mushroom-shaped velocity deficit region around the symmetry plane. The flow topology at x/h = 5 reveals the formation of a saddle point at approximately y/h=0.2 where the flow in the region below the saddle point is directed towards the wall. Downstream at x/h = 15, a second pair of vortices appears at the bottom of the primary pair with opposing rotating direction after the latter has moved upwards under the self-induced motion.

High momentum fluid directs downwards below the saddle point forming a high speed region.

The near wake flow pattern behind the cylinder (Figure 3(b)) differs from the ramp at x/h =5 in which is dominated by a pronounced counter-rotating vortex pair bounding the cylinder (z/h=±1.5, y/h=0.3). The separation between the vortices is 3h. The vortex pair is assumed to result from a horseshoe vortex system upstream of the cylinder (Iyer et al. 2013). Downwash motion is induced resulting in two high speed regions at z/h=±1.0. Lateral upwash produced by the primary vortex pair generates low speed regions and evident velocity deficit. A saddle point at y/h=0.6 is formed at the symmetry plane. The flow below the saddle point moves upwards producing velocity deficit. Downstream to x/h=15, the primary vortex pairs moves upward to y/h=0.6. On the other hand, the spanwise location of the vortex core stays constant. The velocity deficit at the symmetry plane becomes much weaker due to the effect of the central downwash motion of the primary vortex pair.

Similar to the vortical structure downstream of the cylinder, the primary horseshoe originated vortex pairs are present at x/h=5 downstream of square (Figure 3(c)). The spanwise separation of the vortex pair has increased by 0.6h compared to cylinder. The velocity deficit at the symmetry plane is relatively weak. Downstream at x/h=15, besides wall-normal movement, the primary vortices also undergoes spreading process in spanwise direction.

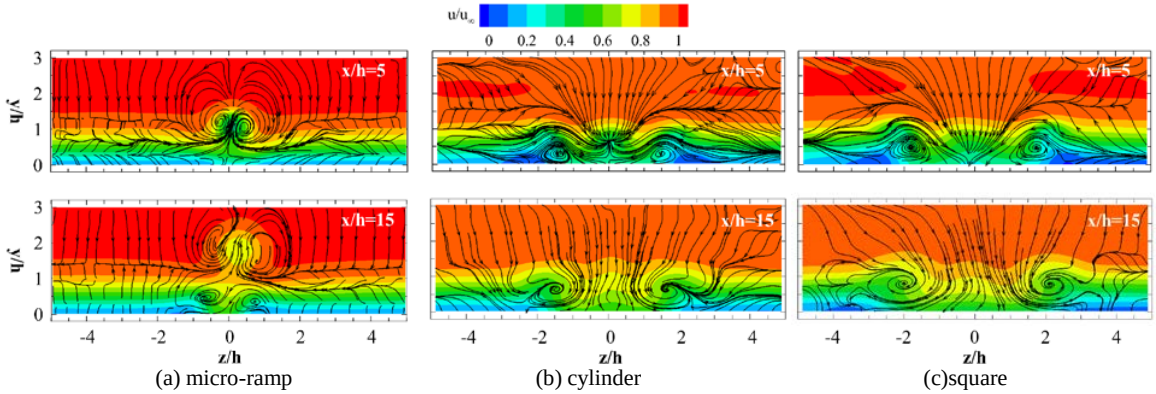

(a) micro-ramp (b) cylinder (c)square

Figure 3 Contour of streamwise velocity (u/u_∞).

VELOCITY FLUCTUATIONS

An increased level of velocity fluctuation is expected in the wake of roughness elements compared with that of the undisturbed boundary layer. The velocity fluctuations are depicted by the RMS of the streamwise velocity component ($\langle u' \rangle / u_\infty$) at six y-z cross-sections shown in Figure 4. The y-z cross-section contours are lined with averaged streamwise velocity.

In the near wake of micro-ramp (x/h<15), instantaneous upwash induced by the primary vortex pair contributes to strong streamwise velocity fluctuation at the wake center and interface of the wake and the freestream motion. The downwash motion produced by the secondary vortex pair transport high momentum fluid to the near wall region, resulting in high streamwise velocity fluctuation near the wall. The maximum velocity fluctuation decreases when travelling downstream due to wake recovery. Downstream at x/h=30, the velocity fluctuation induced by the primary vorties completely fades out. However, the near wall velocity fluctuation sustains strong. Besides, away from the wall at y/h=1, two symmetrical peaks of streamwise velocity fluctuation shown on top of the low speed blob. Further downstream, the cross-sectional area interested by fluctuations has increased both along spanwise and wall-normal direction and resembles a wedge shape, indicating the onset of a turbulent wedge. A homogeneous distribution of streamwise velocity fluctuation can be observed near the wall in the wedge center. The symmetrical peak at y/h=1 persists downstream at the border of the turbulent wedge.

The strongest streamwise velocity fluctuation in the near wake of cylinder is concentrated at the interface of three low speed regions and the freestream. The inflectional velocity profile at the symmetry plane suggest that the median peak results from K-H instability. The other two peaks away from the symmetry plane is caused by the lateral upwash motion of the primary vortices, which induces strong momentum transport. Moving downstream, peak at the symmetry plane undergoes fast recovery process and cannot be observed at x/h=30. Whereas the lateral peaks remains strong and persists downstream with decreasing intensity. Large spanwise spreading of the interested area of fluctuation can be observed, which remarks the onset of turbulent wedge. Opposing to the homogeneous distribution of streamwise velocity fluctuation at the center of turbulent wedge, two symmetrical peaks locates at the border of turbulent wedge also keep active till the most downstream region.

Comparing to cylinder, the velocity fluctuation in the downstream of square also shows triple peaks in the near wake. The onset of turbulent wedge in the downstream can be observed with a larger area of velocity fluctuation activity. High velocity fluctuation focuses at the border turbulent wedge.

The formation of turbulent wedge indicates that late stage transition happens in the roughness wake. Strong velocity fluctuation at the border of the turbulent wedge is

assumed to contribute to the transport of the unsteadiness from the turbulent core to the laminar region. Detailed flow pattern of the turbulent wedge will be analyzed in the next section. The spreading angle of the turbulent wedge in the wake of miro-ramp, cylinder and square is 4.5˚, 5.3˚ and 6.1˚ respectively, indicating an increase of the spatial growth of turbulent region.

INSTANTANEOUS FLOW ORGANISATION

With an incoming laminar boundary layer interacting with roughness element, the sources of unstable oscillation reveals different transition mechanisms behind various roughness elements. Whether transition is driven by the instabilities in the separated shear layer or the streak flow behind the roughness element is not well understood yet. The present experiments visualize the instantaneous three-dimensional vortical structure detecting by λ_2 criterion in Figure 5. Additionally, the chosen iso-surface is color-coded by streamwise velocity to better distinguish the regions of accelerated and decelerated flow. The blue line indicates the location the core of averaged streamwise vortices.

In the wake of the micro-ramp (Figure 5(a)), the flow fluctuations due to the growth of Kelvin-Helmholtz rollers becomes visible behind $x/h = 5$ with arc-shape vortices spaced at regular intervals of approximately $\lambda/h = 1.4$. When convecting downstream, the vortices appear elongated and hairpin-like, due to the continuity of circulation from the head towards the legs, mostly due to the presence of the primary vortex pair. At x/h=15, the interval of K-H vortices undergo sudden growth ascribed to the vortex pairing mechanism. This process is observed to occur intermittently, and therefore does not lead to doubling the wavelength as evaluated from statistical cross-correlation analysis. Instead, the maximum interval of the vortices reaches λ/h=2.1, which is 1.5 times as the separation observed in the vortex shedding region.

After the pairing region, the vortices rapidly break down under the effect of azimuthal instabilities accelerated by the strain rate of the boundary layer. As a result, the ring shape vortices are distorted and split into fragments. The vortices lose periodicity downstream of $x/h = 25$ and the associated vortex activity has no clear pattern up till $x/h = 35$, where newly formed vortex structures are observed in the near wall region with hairpin shape with head (spanwise rotation) and leg (quasi-streamwise rotation) portion. Unlike the flow topology near the micro-ramp, the vortex structures appear shifted away from the symmetry plane and develop downstream with a spanwise spreading. The hairpin stays in a relatively constant wall-normal position. No clear periodicity can be interpreted from the hairpin vortices. Near the symmetry plane, no apparent activity of large-scale coherent vortex structures is observed indicating a more isotropic turbulent regime

The wake of cylinder and square exhibit similar mean vortex topology as well as instantaneous flow pattern. Only the instantaneous flow organization over cylinder is analyzed in detail for sake of conciseness (Figure 5(b)). From the most upstream region in the measurement domain (x/h=[3,5]), primary hairpin vortex (PHV) are produced at the upper unstable shear layer near the symmetry plane, due to K-H instability. The interval of neighboring PHV is λ/h=3.5, which is 2.5 times larger than the interval exhibited behind the micro-ramp. As the growth rate of the perturbation is inversely proportional to the wavelength of the vortices (Cushman-Roisin. 2014), K-H instability is comparatively less important in the wake of cylinder. Downstream at $x/h = 9$, the upwash motion away from the symmetry plane produces strong ejection events associated to vortices located at the spanwise boundary of convected PHV. Instead of complete hairpin vortex structure, the side vortices (SV) appears more in a cane or leg shape, which is caused by non-uniform stretching, partial tearing, cutting and connecting. The wavelength of SV is $\lambda/h = 1.7$ (half of the initial wavelength of PHV). The SV travels downstream with slight spanwise spreading. Sub-PHV with smaller intensity is generated at x/h=11, which is possibly due to the mutual approach between neighboring vortices. In the range of x/h=[10,15], the neighboring PHV and SV resembles the formation of U-shape vortices, which is described as the early stage of transition (Singer and Joslin. 1994). In the downstream region, PHV loses coherence and periodicity as they appear to undergo strong distortion and break down into pieces. Also in this case the activity of large coherent vortices is visibly weaker and more sparse near the symmetry plane.

A chain of newly induced hairpin vortices can be observed with strong portion of quasi-streamwise hairpin legs aside of SV at x/h=15. The new hairpins also spread spanwise and sustain strong intensity while convecting downstream. The regular interval of SV persists till $x/h = 30$. Further downstream, coherent and periodic SV structures are hardly observed as their intensity becomes weaker and the flow fluctuations start to be dominated by newly generated hairpin vortices.

In the vortical structure of square (shown in Figure 5(c)) the PVS and SV have the same wavelength of $\lambda/h = 2.5$. The U-shape vortex structure can also be detected. Same onset location of newly formed vortices train indicates the onset of transition.

The global scenario of the newly generated hairpin vortices for micro-ramp, cylinder and square shows a wedge shape, signifying a spanwise spatial growth of the vortex structure. Durbin and Wu (2006) reported that the formation of low speed region provides favorable condition for perturbation triggering transition, which is accordant with the condition at the rear face of turbulent spot. Hairpin vortices are also an ubiquitous phenomenon in turbulent spot. Consequently, the formation of turbulent wedge can be confirmed in current experiment, denoting the late stage of boundary layer transition. With sparse coherent structure in the wedge center, the hairpin vortices remains active at the edge of the turbulent wedge, which induces strong velocity fluctuation at the turbulent-laminar interface.

CONCLUSION

The three-dimensional organization of the boundary layer undergoing transition under the effect of isolated roughness elements (micro-ramp, cylinder and square) is investigated at supercritical roughness-based Reynolds

number (Re_h) using Tomographic PIV. The measurement resolution enables the analysis of the time-averaged flow topology where various systems of streamwise vortices are identified, which play a role in the inception of the flow instability. The current measurements have also enabled the detailed analysis of the instantaneous flow pattern with the detection of unsteady growing waves and hairpin vortices developing along the transition region.

In the wake of roughness elements, the hairpin vortices associated to K-H instability starts to be active in the upstream region of the wake center but do not seem to be directly connected to the onset of transition as they move upwards rapidly and undergoes fast distortion process. The hairpin vortices plays an important role in the propagation of unsteadiness at the laminar-turbulence interface. The onset of transition and lateral spreading of turbulent fluctuations in the micro-ramp flow is significantly delayed in comparison to the case of the cylinder and the square. The sideward hairpin vortices formed away from the symmetry plane in the wake of the cylinder and square obstacles appear to directly lead to the formation of newly generated hairpin vortices, which accelerates the onset of turbulent wedge and boundary layer transition.

REFERENCE

Acarlar, M.S., and Smith, C.R., 1987, "A Study of Hairpin Vortices in a Laminar Boundary Layer. Part 1. Hairpin Vortices Generated by a Hemispherical Protuberance", *Journal of Fluid Mechanics*, Vol. 175, pp. 1–41.

Choudhari, M., Li, F., Wu, M., Chang, C-L., Edwards, J., Kegerise, M., King, R., 2010, "Laminar Turbulent Transition behind Discrete Roughness Elements in a High-Speed Boundary Layer", AIAA-2010-1575.

Cushman-Roisin, B., 2014, "Environmental Fluid Mechanics", John Wiley & Sons, Inc, USA, pp103.

Danehy, P.M., Ivey, C.B., Inman, J.A., Bathel, B.F., Jones, S.B., McCrea, A.C., Jiang, N., Webster, M., Lempert, W., Miller, J., Meyer, T., 2010, "High-Speed PLIF Imaging of Hypersonic Transition over Discrete Cylindrical Roughness", AIAA 2010-703.

Durbin, P., and Wu, X., 2007, "Transition Beneath Vortical Disturbances", *Annual Review of Fluid Mechanics*, Vol. 39, pp. 107-128.

Ergin, F.G., and White, E.B., 2006, "Unsteady and Transitional Flows Behind Roughness Elements", *AIAA Journal*, Vol. 44(11), pp. 2504–2514.

Iyer, P.S. and Mahesh, K., 2013, "High-speed Boundary-layer Transition Induced by a Discrete Roughness Element", *Journal of Fluid Mechanics*, Vol. 729, pp. 524-562.

Klebanoff, P.S., Cleveland, W.G., and Tidstrom, K.D., 1992, "On the Evolution of a Turbulent Boundary Layer Induced by a Three-dimensional Roughness Element", *Journal of Fluid Mechanics*, Vol. 237, pp. 101–187.

Li, Q., and Liu, C., 2010, "LES for supersonic ramp control flow using MVG at M=2.5 and Re_θ=1440", AIAA 2010-592.

Rizzetta, D.P., and Visbal, M.R., 2007, "Direct Numerical Simulation of Flow Past an Array of Distributed Roughness Elements", *AIAA Journal*, Vol. 45(8), pp. 1967-1976.

Singer, B.A., and Joslin, R.D., "Metamorphosis of a hairpin vortex into a young turbulent spot" , *Physics of Fluids*, Vol. 6(11), pp. 3724-3736.

Sun, Z., Schrijer, F.F.J., Scarano, F., and van Oudheusden, B.W., 2012, "The Three-dimensional Flow Organization Past a Micro-ramp in a Supersonic Boundary Layer", *Physics of Fluids*, Vol. 24(11), pp. 1-22.

Tirtey, S. C., Chazot, O., and Walpot. L., 2011, "Characterization of Hypersonic Roughness-Induced Boundary-Layer Transition", *Experiment in Fluids*, Vol. 50, pp. 407–418.

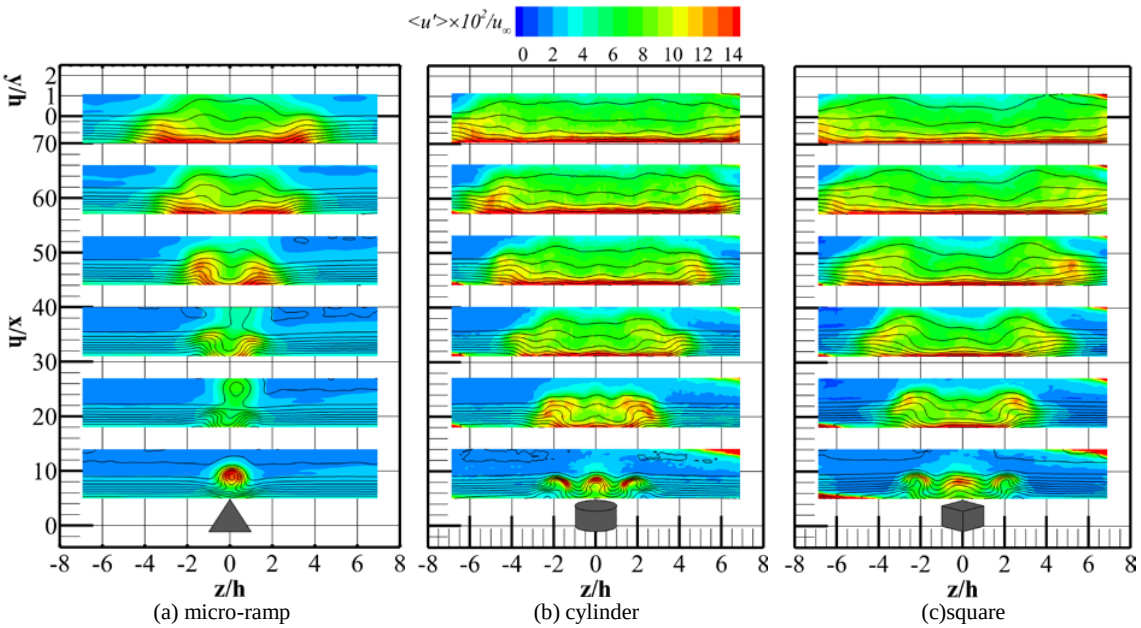

(a) micro-ramp (b) cylinder (c)square

Figure 4. *y-z* cross-sectional contour of streamwise velocity fluctuation $<u'>/u_\infty$.

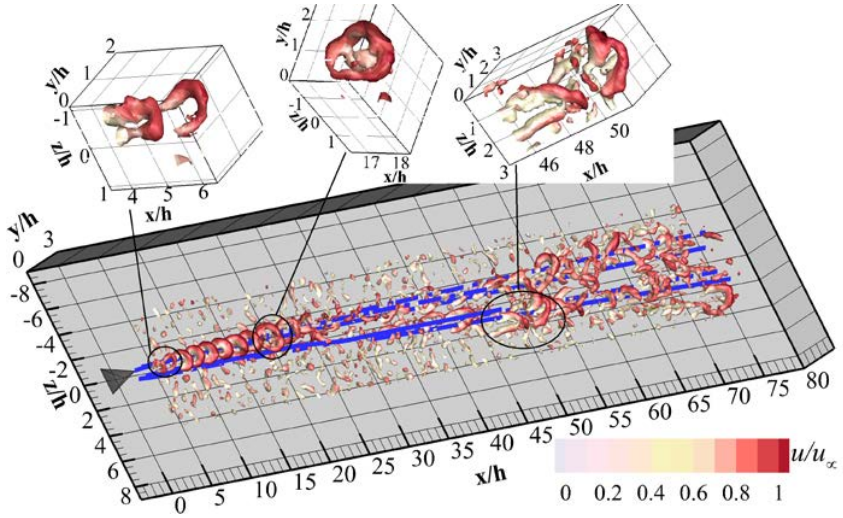

(a) micro-ramp

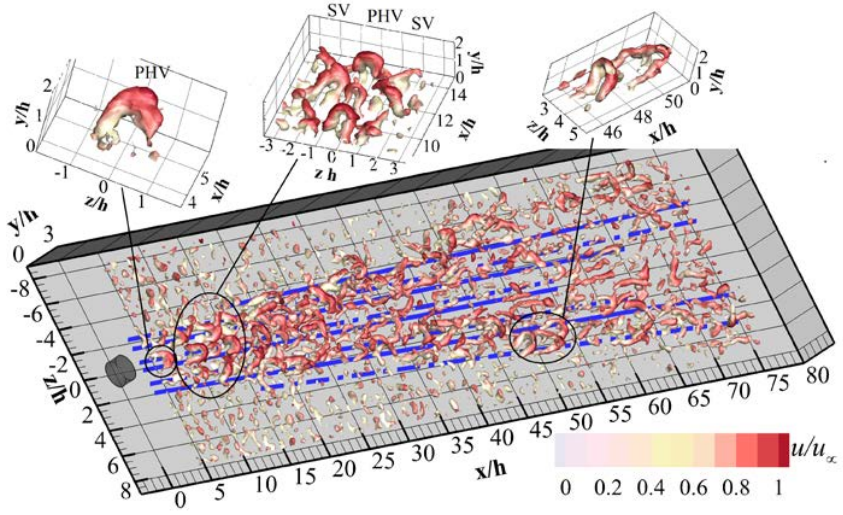

(b) cylinder

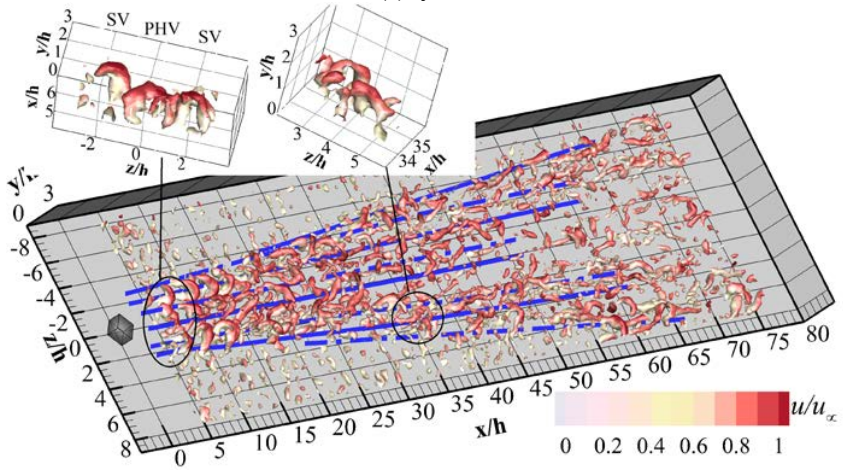

(c) square

Figure 5 The instantaneous flow pattern shown by λ_2 criterion, color coded by u/u_∞;
Solid blue line: clockwise rotating streamwise vortices, dash dot blue line: anti-clockwise rotating streamwise vortices